



**HAL**  
open science

# Optimization of pore-network characterization of a compacted clay material by TEM and FIB/SEM imaging

Stéphane Gaboreau, Jean-Charles Robinet, Dimitri Prêt

## ► To cite this version:

Stéphane Gaboreau, Jean-Charles Robinet, Dimitri Prêt. Optimization of pore-network characterization of a compacted clay material by TEM and FIB/SEM imaging. *Microporous and Mesoporous Materials*, 2016, 224, pp.116 - 128. 10.1016/j.micromeso.2015.11.035 . hal-01690744

**HAL Id: hal-01690744**

**<https://brgm.hal.science/hal-01690744>**

Submitted on 5 Dec 2022

**HAL** is a multi-disciplinary open access archive for the deposit and dissemination of scientific research documents, whether they are published or not. The documents may come from teaching and research institutions in France or abroad, or from public or private research centers.

L'archive ouverte pluridisciplinaire **HAL**, est destinée au dépôt et à la diffusion de documents scientifiques de niveau recherche, publiés ou non, émanant des établissements d'enseignement et de recherche français ou étrangers, des laboratoires publics ou privés.



## Optimization of pore-network characterization of a compacted clay material by TEM and FIB/SEM imaging



Stéphane Gaboreau <sup>a, \*</sup>, Jean-Charles Robinet <sup>b</sup>, Dimitri Prêt <sup>c</sup>

<sup>a</sup> BRGM, Environment and Process Division, 3, Avenue Claude Guillemin, F-45060 Orléans Cedex 2, France

<sup>b</sup> Andra, 1/7 Rue Jean Monnet, Parc de la Croix Blanche, 92298 Châtenay-Malabry Cedex, France

<sup>c</sup> UMR CNRS 7285 IC2MP, Université de Poitiers, Equipe HydrASA, Rue Albert Turpain, Bat B8, 86022 Poitiers, France

### ARTICLE INFO

#### Article history:

Received 23 September 2014

Received in revised form

20 October 2015

Accepted 9 November 2015

Available online 30 November 2015

#### Keywords:

Clay

Microstructure

Pore size distribution

FIB nanotomography

Porosity

### ABSTRACT

In clay-rich sedimentary rocks, the pore network is considered to play a key role in controlling transport properties. The pore size distribution (PSD) of clay-rich rocks, the geometrical features of the pore network, and the clay content are parameters governing the diffusion process through clay formations. In the last few years, research has contributed to improving understanding of some clay-rich rock pore networks by using microscopic imaging techniques (FIB-nt, BIB, X-ray tomography, etc.). These techniques image the mesostructure scale organization of clay materials, but the studies have highlighted several limitations for full pore distribution characterization in terms of geometry and connectivity. Here we demonstrate that we can characterize a clay material's pore network supported by FIB-nt and TEM techniques reliably, to provide useful input data for assessing a future modeling task. The material studied was a compacted clay material mainly composed of illite, a non-swelling mineral. Illite was chosen in order to represent an analog system mimicking the clay matrix of natural clay-rocks. With this compacted clay plug we were able to work on homogeneous systems with controlled porosity, facilitating comparison between different methods. All the techniques used in this work, whether bulk or microscopic, show that all results converge to a similar and full PSD. This project's main improvement was to demonstrate how to improve the usual resolution limitations and data handling of FIB-nt techniques in order to recognize a fully connected pore network.

© 2015 The Authors. Published by Elsevier Inc. This is an open access article under the CC BY-NC-ND license (<http://creativecommons.org/licenses/by-nc-nd/4.0/>).

## 1. Introduction

In the field of radioactive waste repository, clay-rich rock formations are envisaged as barrier materials due to their favorable properties (low permeability, high radionuclide retention capacity, low diffusion coefficients for solute species, swelling properties, etc.) [1,2]. The transport properties of clay-rocks are controlled by their complex pore network and reactive and negatively-charged clay mineral surfaces. In clay-rich rocks, pore size distributions (PSD) typically range between nanometer and micrometer with dominant pore size diameters around tens of nanometers; these correspond to mesopores [3–5]. The co-occurrence of nanometer-sized pores and clay mineral charged surfaces induces specific macroscopic solute transport behaviors such as anion exclusion (*i.e.* anion mobility lower than for water molecules) and enhanced

cation diffusion (*i.e.* cation mobility higher than for water molecules) [6–9]. Though both these phenomena have been relatively well observed at the macroscopic scale using diffusion experiments on anionic and cationic tracers with associated bulk macroscopic modeling approaches, an integrated modeling approach from the pore scale to the pore network scale is still required to build up a robust bottom-up strategy to support performance assessment for a radioactive waste repository. One of the main reasons for this gap is the lack of robust small-scale representations of the pore network and the associated mineral distribution for clay-rich rock materials. On the other hand, 2D and 3D imaging techniques (TEM: *Transmission Electron Microscopy*, *Focused Ion Beam - Scanning Electron Microscopy nanotomography (FIB/SEM nt)*, X-Ray tomography, electron probe-based X-ray maps, autoradiograph porosity mapping, etc.) have recently demonstrated the possibility of extracting quantitative key parameters about clay-rich material organization [10–21]. These studies have however emphasized that a single imaging method is not able to fully encompass pore networks having PSD ranging between nanometers and micrometers

\* Corresponding author.

E-mail address: [s.gaboreau@brgm.fr](mailto:s.gaboreau@brgm.fr) (S. Gaboreau).

mainly due to the dual limitations of the spatial resolution with the associated field of view (FOV) specific to each method. Uncommon previous research has attempted to combine several techniques (X-ray tomography, FIB-nt and TEM) to encompass the full PSD from largest to smallest pores of a clay material [16]. The PSD obtained at each scale with the different techniques do not successfully match in the overlapping scale ranges, clearly indicating that the PSD obtained are not cross-validated. For shale, the anisotropic distribution of the minerals and pores is so scattered that it is quite difficult to compare each technique as the porosity information obtained by FIB-SEM could strongly varied among the heterogeneous facies of that shale [22]. Technical limitations (spatial resolution/FOV pair regardless of the Representative Volume Element (RVE) of each method used) are usually stated to explain these differences, neglecting that strong bias could be involved by varying sample preparation, the choice of acquisition parameters and the image analysis approach used. In the data handling, the pore network recognized and its volume are strongly impacted by the segmentation approach used when basic thresholding approaches are used [23,24]. The actual distribution of pores and minerals in natural shales is the result of overlapped and successive processes of mineral growth and dissolution as well as localized compaction steps throughout the geological history of the rock. Therefore, rock organization is strongly heterogeneous at each scale and obtaining perfect matches for the results of different methods applied on various sampled volumes is not straightforward. This is indeed currently a scientific bottleneck to properly implementing a multi-scale strategy to directly model solute diffusion on real pore networks of clay-rocks and better understand their specific diffusion properties.

In this study, we propose integrated methodology to characterize mineral and pore spatial distributions of clay-rich materials from nanometers to micrometers. This work focuses on compacted mesoporous illite samples (a simpler model system than natural clay-rock) in the hopes of extending our findings to natural clay-rich rock formations. Illite was chosen because it is the main constituent of the clay-rock porous matrix as swelling clay contents are very low [25] and other minerals such as carbonates and quartz are non-porous in clay-rocks [19]. Compacted illite samples mimic the mesoporous clay matrix constituting clay-rocks well. This analog system has been studied previously for several purposes such as hydraulics, diffusion, radionuclide sorption and mechanical properties [7,26,27]. Our approach is mainly based on imaging the nano-microscale organization ( $\mu\text{m}$ - $\text{nm}$ ) of compacted illite materials using TEM and FIB/SEM-nt imaging techniques and analyzing the resulting set of images to extract quantitative information on pore space, mineral spatial distributions, and morphology. The methodology we propose aims to improve several key steps including the sample preparation, image acquisition, image analysis and the final quantification of the PSD, by cross-validating the results from bulk techniques. Such a comparison is possible through the use of samples more homogeneous than natural clay-rock. Finally, the work validated a method of image analysis based on FIB and TEM data on more homogeneous and non-swelling clay materials whereby we could compare bulk and image-based PSD applied on various sample volumes. This method of FIB-nt data acquisition and image analysis can therefore be applied with confidence to more heterogeneous clay materials according to the probed volume.

## 2. Material and methods

### 2.1. Illite du Puy (IDP)

Illite mineral is a non-swelling clay made of 1 nm thick aluminosilicate 2:1 layers [28]. For the sake of this study, IDP was used as a

reference illite phase [27]. IDP is extracted from Eocene lacustrine continental sediments in the Le Puy en Velay basin (Massif Central, France). This sedimentary formation is mainly composed by illite clay minerals (80–100%). In association with illite, kaolinite is identified as a clay mineral phase with proportions ranging from 0 to 20% of the clay fraction [29]. Because of its sedimentary nature, the clay-rich Puy en Velay formation also contains non-clay minerals such as carbonate, K-feldspar and quartz, present in varying amounts (between 0 and 40%). Consequently, a purification procedure is required to extract the illite reference material from the raw geological formation. This is to remove the non-clay components of the rock and increase the amount of illite at the expense of kaolinite. Baeyens and Bradbury [30] have recommended a standardized procedure for the purification in numerous studies. After this treatment, the amount of illite is ~88–93%, with a variable amount of kaolinite. In our study, the raw material was purified according to this procedure. After treatment, powder X-ray diffraction revealed that the amount of illite was ~85–90%, and that K-feldspar was present. Complementary oriented X-ray diffraction analyses have also highlighted that the purified IDP material contains an illite/smectite mixed layer fraction (~20–30% of the clay fraction) with a low smectite layer content in the mixed layer structure (1/S in a proportion of 80/20). Finally, the purified material was composed of illite layers (90–94%) and negligible smectite layer (4–6%) and K-feldspar (less than 5%) contents while in natural clay-rock like Callovo-Oxfordian clay-rock (Bure, ANDRA URL), the clay fraction is composed of more than 50% illite and approximately 20% smectite layers mixed with various amount of chlorite and kaolinite [31].

### 2.2. Sample preparation

The dry, crushed, purified illite powder was first sieved at 100  $\mu\text{m}$  and then compacted, using a hydraulic press at dry bulk density of 1.7  $\text{g}/\text{cm}^3$  corresponding to a bulk porosity of 39% when considering the solid density of 2.78  $\text{g}/\text{cm}^3$  measured by helium pycnometry. This compaction density was selected in order to mimic the specific porosity of clay-rock clay matrix [20]. The sample size was fixed at 35 mm in diameter and 10 mm thick.

Smaller samples dedicated to bulk measurements were then frozen in slush nitrogen freeze-dried before storing then under vacuum for their analysis [17]. Note here that the low content in swelling-clay minerals with smaller particle sizes limits the potential drying/shrinkage damages.

The samples were then placed in cells to ensure mechanical confinement and constrain the sample volume upon rehydration or impregnation processes. For electron beam-based imaging methods applied under vacuum, resin impregnation is conventionally setup for sample preparation. In this work, the methylmethacrylate (MMA) resin impregnation method was implemented in order to preserve the texture in a water-like saturation state without losing the clay confinement or modifying the pore space geometry during sample manipulation (sectioning, polishing, and image acquisition). The works of [3] and [17] have proved the efficiency of MMA pure monomer-based resin for fully impregnating clayey materials (low viscosity, dipole moment similar to water, small size molecules). Details about this technique can be found in Refs. [3,11,12,17,18,21,32]. MMA impregnation lasted 2 months so that the pore space was fully saturated. After this period, MMA was polymerized through the addition of a thermal initiator by heating at 60 °C. After this step, the impregnated IDP samples could be handled without damaging their microstructure. These samples were used to prepare subsamples of polished thick sections for multi-technique image acquisition.

### 2.3. Pore space characterization by bulk techniques

In addition to imaging techniques, pore space characterizations were performed on bulk freeze-dried IDP bulk samples based on classical nitrogen adsorption/desorption isotherms at 77 K coupled with the BJH method and the mercury intrusion porosimetry (MIP) technique. It is well known that the PSD stem from these methods are based on the interpretations of the raw data in particular the assumptions about pore morphology [33,34] but they remain extensively used to characterize the mesopore distribution down to 2 nm.

On the same samples, nitrogen adsorption/desorption isotherms were measured using a Micromeritics ASAP 2020 volumetric setup and MIP measurements using a Micromeritics Autopore IV 9500. Data obtained from the nitrogen adsorption isotherms was interpreted on the basis of the Kelvin equation linking the partial pressure of gas to the pore radius, assuming pores as cylinders [35]:

$$\log\left(\frac{P}{P_0}\right) = \frac{-2\sigma V_N}{RT} \cdot \frac{1}{r_p}$$

where  $\sigma$  is the surface tension,  $V_N$  the molar volume of liquid nitrogen,  $R$  the gas constant and  $T$  the absolute temperature in K. Taking into account the thickness ( $t_{\text{layer}}$ ) in nm of the multilayer liquid nitrogen adsorbed on the pore walls at a relative pressure interval provided by the Hasley's equation, this leads to the following expression of the pore diameter  $d_p$  [36]:

$$d_p = 2(r_p + t_{\text{layer}})$$

$$\text{With } t_{\text{layer}} = 3.54 \left[ \frac{-5}{\ln \frac{P}{P_0}} \right] 0.33.$$

The PSD was finally estimated using the BJH formalism described by Barrett, Joyner and Hallenda [35], integrating the pore diameter on the adsorption branch for each relative pressure interval. Using this model, PSD were calculated for pore diameters ranging between 2 and 100 nm.

MIP tests were interpreted using both analytical and numerical approaches. The analytical approach is based on the Washburn equation [37] linking the applied pressure of mercury to the pore radius of pores filled by mercury at each step (intrusion or extrusion):

$$r = \frac{2\gamma \cos\alpha}{P}$$

where  $r$  is the entrance pore radius,  $\gamma$  the surface tension of the mercury, and  $\alpha$  and  $P$  are the contact angles of the Hg/air interface on solid and the pressure difference across the interface, respectively. The Washburn equation is valid for pores having a circular cross section, which is the most commonly used pore shape. A more general expression for pores of other shapes such as elliptical or slit can be used by introducing a shape factor into the Washburn equation [38]:

$$d_p = f \frac{\gamma \cos\alpha}{P}$$

where  $d_p$  is the pore diameter and  $f$  the shape factor. The shape factor varies from 2 for slit (parallel walls) pores to 4 for cylindrical pores having a circular cross section [39]. This interpretation is classically considered to be limited since mercury progressively

invades the pore network from the external surface of the sample to its core.

In order to improve the interpretation MIP tests, a numerical program called XDQ [40,41] was used. The XDQ program is based on a multi-scale percolation system for which isotropic constitutive pore networks' structure with cubic lattice and bond percolation has been adopted. Mercury percolation simulations based on a multi-scale pore network model were performed to test several scenarios providing the best pore network (and the resulting PSD) that meant we could reproduce both the mercury intrusion and extrusion curves.

### 2.4. Pore space characterization by imaging methods

#### 2.4.1. Transmission electron microscopy

TEM observations were performed on ultrathin sections. Slices of MMA impregnated IDP, ranging from 50 to 100 nm thick, were cut parallel to the axis of compaction using a Leica UC7 ultramicrotome equipped with a diamond knife. TEM 8-bit grayscale images ( $4008 \times 2672$  pixels) were then acquired on a Philips CM20 microscope, operated at 200 kV, with a point resolution of 0.14 nm. Low magnification bright-field images were recorded to visualize the millimeter to micrometer scale organization of the compacted IDP samples. Selected representative areas were also acquired at higher magnification to depict the nanometer scale organization (clay particle morphology, pore/clay interface, illite clay internal structure). Illustration of the successive down-scaling bright-field images of compacted illite are displayed on Fig. 1. In TEM images of such pure illite samples, grayscale intensity depends mainly on the local electron density, which is related to local porosity values (dark pixels correspond to pure solid, bright pixels to pore and intermediate grayscale to a mixture of pores and solid).

#### 2.4.2. Focus ion beam nanotomography

FIB-nt was done with a dual-beam SEM instrument. The principle of the FIB-SEM-nt approach is detailed in Ref. [42] and basically corresponds to successive milling of a thin sample layer by a gallium beam followed by SEM imaging. Images were acquired on a Zeiss NVision 40 equipped with a GEMINI® e-beam FESEM column technology with two in-lens detector systems for ultra-high resolution imaging. The SEM was operated at a low acceleration voltage of 1.7 keV and a dwell time/pixel of 0.2  $\mu$ s. Ion gun milling current was at 300 pA. The GEMINI® column design includes an integrated in-lens secondary electron (SE) detector and a second in-column detector enabling simultaneous detection of backscattered electrons (BSE) with an EsB grid to select the range of detected BSEs according to the landing energy. The ULTRA FESEM with the dual in-column detectors enables simultaneous ultra-high resolution imaging with secondary and backscattered electrons at lower accelerating voltage in comparison to a classical BSE detector. Low voltage BSE imaging with the EsB detector allows the acquisition of images with a better signal to noise ratio than the SE ones and with both better lateral resolution and an escape depth smaller than 5 nm (Fig. 2). The energy filtering of the EsB detector makes it possible to select only BSE with low loss energy emitted on an area of the sample surface close to the electron probe size, i.e. smaller than 5 nm. For this purpose, millimetric impregnated subsample specimens were prepared with a diamond saw (thickness of the saw blade = 100  $\mu$ m) for the FIB-nt acquisition. The cross-sections were cut perpendicular the compaction axis. A cube size of 1 cm<sup>3</sup> was prepared to assess it. The cross-section surface was polished for 2 h with fine-grained (1/4  $\mu$ m) diamond powder. Two stacks of 180 SEM 8 bit encoded images with dimension  $2048 \times 1536$  pixels were recorded. The pixel size in the 2D images is  $5 \times 5$  nm<sup>2</sup>. Between the images, a layer of 5 nm thickness was milled away. Thus,

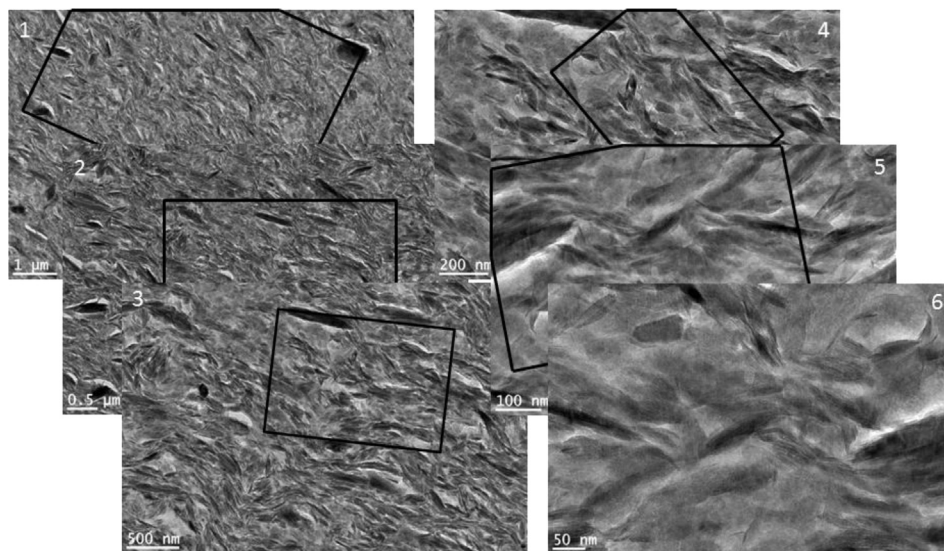


Fig. 1. TEM images of compacted IDP. Down-scaling illustrations (from 1 to 6) of compacted IDP organization.

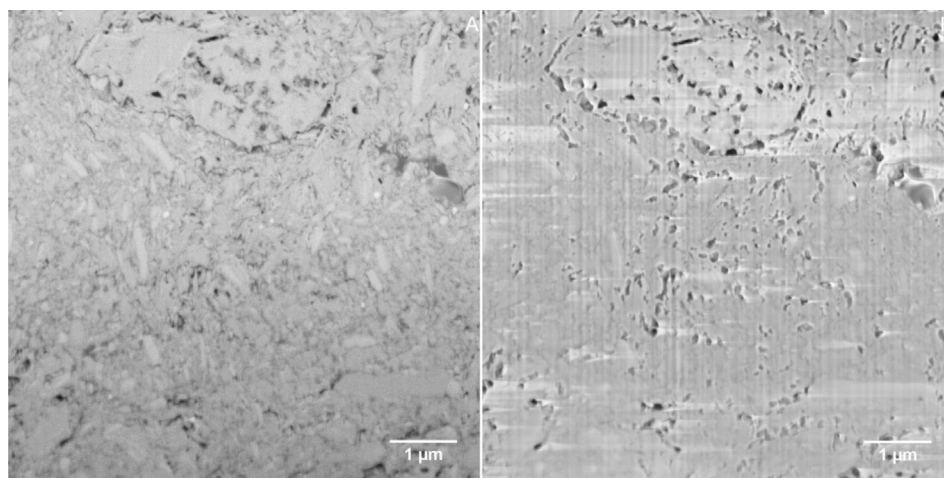


Fig. 2. EsB (A) and secondary (B) electron images obtained simultaneously with the dual in-column detector of the ULTRA FESEM GEMINI® column.

one voxel in the 3D data set represents volume of  $5 \times 5 \times 5 \text{ nm}^3$ . The FIB/SEM volume presented is a cropped subvolume (size  $1404 \times 1404 \times 180$  pixels) of the total block of materials analyzed, which is focused on a region of interest after the stack is aligned. Contrary to TEM images, dark pixels correspond to voids and intermediate grayscale to solid (Fig. 2).

#### 2.4.3. Image analysis

- Textural characterization from TEM images

TEM grayscale images can provide quantitative information about the microstructure of compacted IDP. In the literature, different mathematical tools are proposed to analyze the texture of grayscale images [43]. For our purposes, specific features of the texture were targeted: anisotropy, spatial correlation, and size of a representative pattern.

Spatial distribution properties were first analyzed using a classical semi-variogram function. Semi-variogram characterizes in a given direction the local relation between two pixels separated by a

distance  $h$ . The semi-variogram  $\gamma(h)$  is computed from the following equation:

$$\gamma(h) = \frac{1}{2N} \sum_{x=1}^N (Z_x - Z_{x+h})^2$$

where  $Z_x$  and  $Z_{x+h}$  are the grayscale values of the pixels  $x$  and  $x+h$  separated by distance  $h$  and  $N$  is the number of analyzed pixels to calculate  $\gamma(h)$ . For a non-periodic texture, semi-variogram  $\gamma(h)$  evolves to an asymptotic maximum indicating the loss of correlation between pixels separated by distance  $h$ . The distance to reach the asymptote is related to the size of objects composing the image. Moreover when the semi-variograms are computed for several directions, the anisotropy properties of these objects can be analyzed.

- Preprocessing step for the FIB/SEM raw data

Raw FIB/SEM data requires pre-processing treatments to remove artifacts and analyze them in terms of a 3D volume [13].

The following set of operations was considered and applied using the public-domain software ImageJ (<http://rsb.info.nih.gov/ij/>) and associated open-source plugins:

- i. Due to the specific geometry of the FIB/SEM column (tilting angle between the imaged surface and the electron beam) a non-uniform illumination induces a shadowing effect, corrected with a rolling ball algorithm [44].
- ii. Aligning the stack of images to reconstruct a continuous 3D volume. [Prill, Schladitz, Jeulin, Faessel and Wieser [45]] mentioned that since the segmentation method relies on the analysis of the intensity profile of one pixel in the z-direction (perpendicular to the milling direction), a very precise alignment is necessary to ensure the precise overlap of the images in the stack even to sub-pixel precision. The stack alignment was performed using the affine stack Alignment algorithm provided by the StackReg plugin implemented in ImageJ [46].
- iii. Removing the ‘curtaining’ artifact (vertical stripes) from gallium beam scattering and out-of-plane imaging which is common on the SE images (Fig. 2). These stripes were eliminated by computing the Fast Fourier transform (FFT). Such directional artefacts were then removed by applying a filter [47] on the 2D power spectrum. The inverse FFT is computed to obtain the filtered image.
- iv. Image quality was also enhanced by applying (i) a contrast and brightness adjustment spreading the grayscale histogram and (ii) a Gaussian 3D filter (standard deviation of 2 pixels) to reduce noise.

The different preprocessing steps are illustrated in Fig. 3.

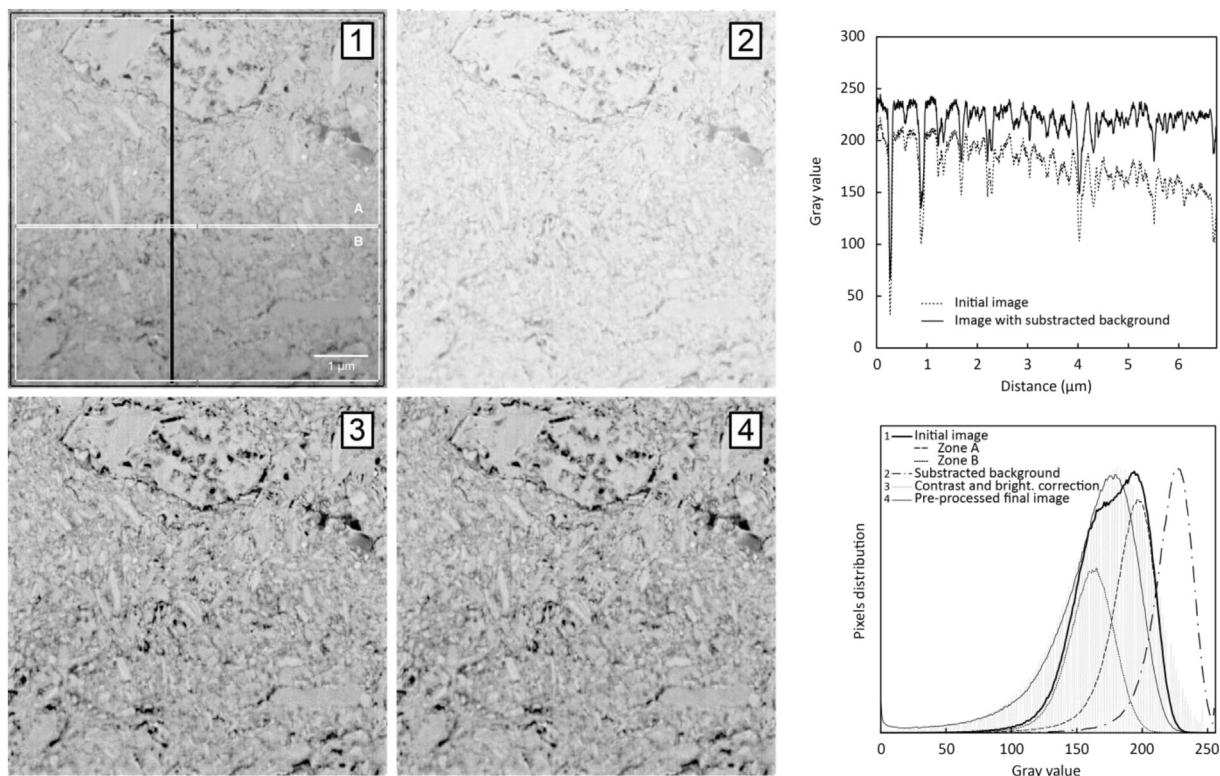


**Fig. 3.** Preprocessing method to improve the signal to noise ratio of the BSE images. Image (1) is the acquired FIB/SEM image; (2) image with subtracted background; (3) Brightness and contrast corrected image and (4) Noise reducing with Gaussian Blur filter. Grayscale profiles are plotted to illustrate the correction of the shadowing effect. The grayscale histogram frequency displayed the evolution of the pixel distribution from the initial image (thick black line) to the preprocessed one (thin black line).

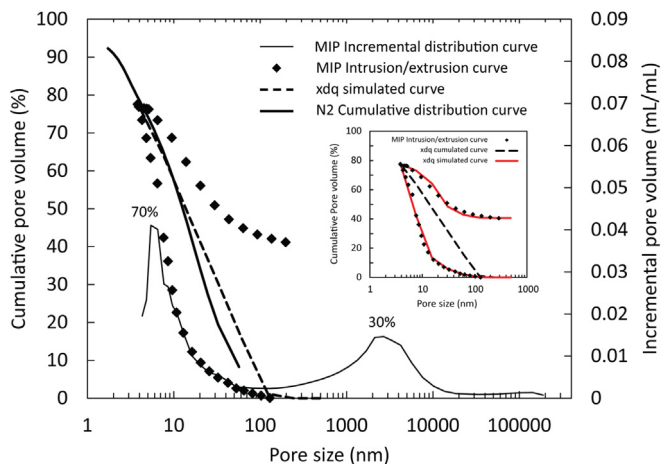


**Fig. 4.** Pore size distributions which were determined with  $N_2$  adsorption and MIP analyses. MIP pore size distribution was calculated with the xdq program (vignette). MIP incremental distribution is presented to illustrate the different class of pore analyzed where the modal distribution centered on  $\mu$ metric size is an artifact of sample preparation.

### 3. Results

#### 3.1. Pore size distribution from bulk measurements

The PSD and the associated probed pore volume were determined by  $N_2$  adsorption and MIP measurement. The cumulative PSD after normalization to the total bulk porosity of 39% for each method were used to determine the probed part of the pore

network. Fig. 4 reveals that more than 90% of the theoretical pore volume was analyzed by N<sub>2</sub> adsorption with pore size diameter ranging from 2 to 100 nm. The raw pore volume investigated by MIP was higher than the theoretical total pore volume. The incremental mercury intrusion curve displays a two mode shape with one mode centered on 5 nm (70% of the MIP pore volume) and another centered on 1–2 μm (30% of the MIP pore volume). The largest pores are unusual and can be attributed to a damaged external sample surface linked to a preparation artifact upon sub-sampling. By removing the pore volume related to this artefact, the cumulative PSD of the undamaged compacted illite can be recalculated upon intrusion and extrusion (Fig. 4). The resulting pore volume probed at the maximum intrusion pressure represents 80% of the theoretical porosity value; this is in a better agreement with limit of resolution of MIP.

The cumulative MIP PSD of the connected pore was modeled by simulating the intrusion and extrusion curves using XDQ software [40,41]. The best match between the simulated and experimental curves was reached when assuming a shape factor corresponding to slit-shaped pores, so perfect simulation of the extrusion curve was not possible. This is because the idealized slit or cylindrical shape of pores and also the isotropic pore network model implemented in xdq do not match the actual complex pore morphology in clay materials. The adjustment made with the shape factor reveals that the PSD calculated with the N<sub>2</sub> adsorption and the MIP are sensitive to the local pore network morphology and is probably less ideal than limiting to slits or tubes (Fig. 4) as well as the involved physics considered in N<sub>2</sub> adsorption and MIP is different. The lonely difference is the total pore volume detected with each technique. The smallest pores detected by MIP are approximately 7 nm whereas the pore sizes detected by BJH are closed to 3 nm smaller with the BJH approach.

### 3.2. Pore network characterization by imaging techniques

#### 3.2.1. RVE estimation and 2D texture analysis based on grayscale TEM images

TEM images were obtained at different FOV (17, 8, 4 μm) with a corresponding pixel size of 4, 2, 1 nm, respectively. For the lower magnification, pores and solid cannot be properly discriminated and thresholded (Fig. 5A, B and C). However, semi-variograms were computed on the grayscale images for 4 directions (0°, 45°, 90° and 135°) on the three TEM images acquired with increasing magnification. For the same direction, the computed semi-variograms are relatively similar, highlighting a similar microstructure probed, whatever the image FOV. The asymptote is reached around 150 nm indicating that the IDP microstructure is composed by objects, pores or particles having a mean size around 150 nm (Fig. 5E). For the same image (FOV 17 μm), semi-variograms computed in the four directions reveal anisotropic behavior in the microstructure with asymptotes reached at 70 nm at 45–90° and 200 nm at 0°. To go further in the interpretations of the semi-variograms, we have performed an analytical adjustment using an exponential law which is the most suitable here (by comparison to Gaussian or spherical models) [48]:

$$\gamma(h) = C \times \left( 1 - \exp\left(-\frac{3h}{a}\right) \right)$$

with C the asymptotic value and *a*, the correlation length. Adjusting the *a* parameter provides a robust estimator of the variation of the semi-variograms in several directions allowing assessment of the texture anisotropy. To a greater extent, modeled semi-variograms like this could be used to feed up-scaling and microstructure modeling [49]. As an example, in the direction of 0° a correlation

length of about 110 nm is obtained for these three TEM images (Fig. 5F). The evolution of *a* with the analyzed directions is given for the three magnifications in a rose diagram (Fig. 5D). Anisotropic behavior is clearly shown for these three images with a ratio around 2 between the highest and the lowest correlation lengths. Note here that maximum and minimum correlation lengths cannot be directly compared due to slight tilting among these three images when the microscope magnification increases. For the three images the lowest correlation length is orthogonal to the highest and corresponds to the compaction axis (Fig. 5A). This behavior indicates preferential orientation of clay particles and the associated pore space during the compaction procedure.

The representative volume element (RVE) (or Representative Surface Element for 2D applications) is defined by Drugan and Willis [50] as 'the smallest material volume element of the composite for which the usual spatially constant macroscopic representation is a sufficiently accurate model to represent mean constitutive response'. In order to estimate the RVE, we propose a method inspired from the work of Galli, Cugnoni and Botsis [51] based on the spatial variability of grayscale mean values computed for various window sizes. For a given radius of window *r*, the standard deviation is calculated as follows:

$$\sigma^2(r) = \frac{1}{N} \sum_{x=1}^N (Z(r)_x - \bar{Z}(r))^2$$

with *Z<sub>x</sub>(r)* the grayscale mean of a window of size *r* centered on the pixel *x* and  $\bar{Z}(r)$  the mean grayscale of all the windows of size *r* (which is roughly equivalent to the mean grayscale of the image). In order to optimize the computation of the grayscale mean values of windows having different sizes, we have successively applied on the image a 'local mean filter' (spherical filter) of different sizes. The local mean filter transforms the grayscale of each pixel into the mean grayscale of a surrounding area (a disc of radius *r*) defined by the filter. The standard deviation is then computed from each filtered image. For the three analyzed TEM images, the standard deviation  $\sigma^2(r)$  according to the evolution of the window size images is relatively similar and in agreement with results obtained from semi-variograms (Fig. 5G). Standard deviations reach a minimum asymptotic close to a radius of 500–600 nm; this corresponds to a surface area of 1 μm<sup>2</sup>. The correlation lengths determined from semi-variograms are smaller by one order of magnitude (110 nm) than the characteristic lengths to reach the Representative Surface Element (diameter of 1–1.2 μm). These two scale lengths are in good agreement with the respective notions of the size of the objects and of their representative spatial arrangement.

#### 3.2.2. 2D segmentation of the pore space distribution on TEM images

The partitioning of pores from a TEM image was carried out for an intermediate level of magnification corresponding to a field of view 3 × 2.4 μm regardless of the previously determined RVE. However partitioning pores in TEM images is not straightforward since TEM does not provide 2D sections but integrates information averaged through the thickness of the ultrathin section. Consequently, pixels in the TEM image mainly correspond to a pore and solid mixture distributed along the thickness of the section. Local changes in pore/solid ratio cause grayscale variation. In a first approximation, as most of the pores are smaller than the thickness of the ultrathin section (~100 nm), TEM images can be seen as a spatial distribution map of local porosity instead of pores. Taking into account these limitations, image segmentation was performed with the objective of identifying three phases: pores, solid (or

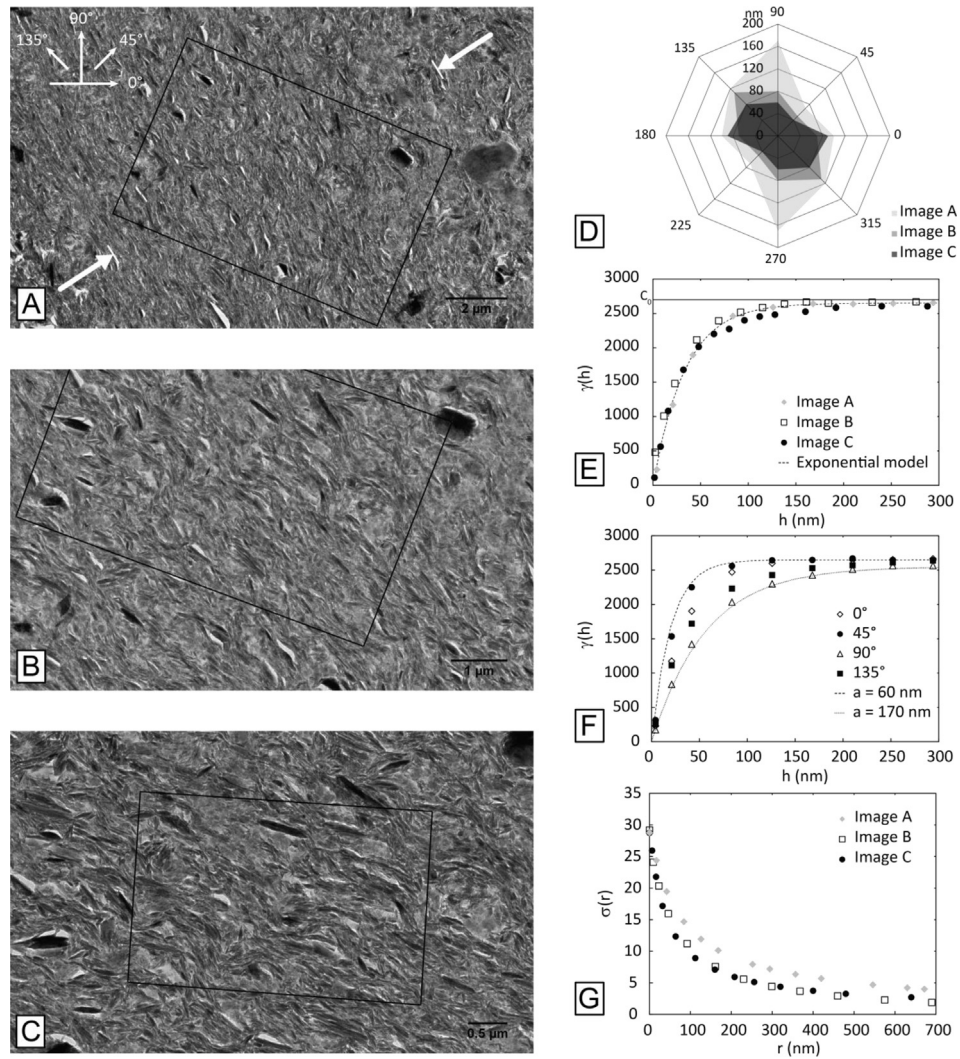


**Fig. 5.** TEM images at different magnification corresponding to field of view of 17  $\mu\text{m}$  (A), 8  $\mu\text{m}$  (B) and 4  $\mu\text{m}$  (C). The orientation grid indicates the rotation of images as a function of magnification and regardless of the compaction axis (white arrows). Orientation (D), variograms (E, F) and covariance (G) calculated on the TEM images.

minerals) and a mixture of pore and solid phases (Fig. 6). These three phases were partitioned using a watershed algorithm [52] provided by the software Aphelion™. In comparison with global threshold value methods, watershed segmentation takes into account local information to enhance the robustness of the

segmentation. First a gradient image is computed to obtain an image with low grayscales (low gradient) in homogeneous regions belonging to pores, solids or mixtures in depth and strong grayscales/gradients at the boundaries of these objects. The principles of the watershed method are as follows, in gradient grayscale

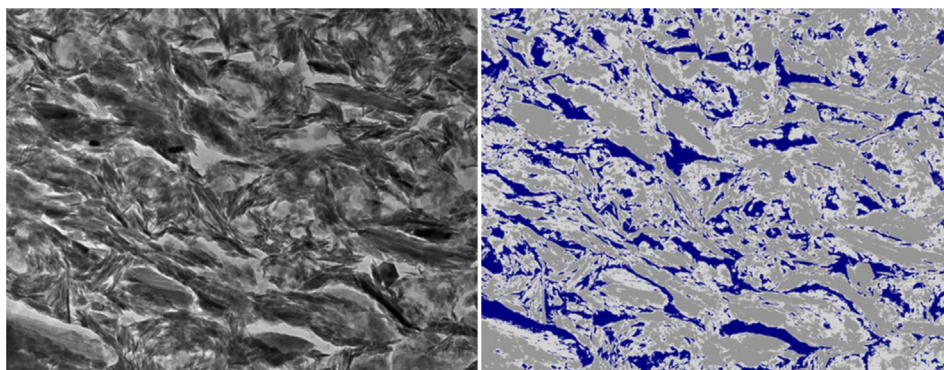


**Fig. 6.** TEM micrograph of compacted IDP and associated segmented image with a field of view of 2  $\mu\text{m}$ . Blue represents pores and light and dark gray are pore/solid mixtures and solids, respectively. (For interpretation of the references to color in this figure legend, the reader is referred to the web version of this article.)

image, where each grayscale is considered as an altitude as in a topographic map, and the watershed algorithm allows the image to be partitioned into homogenous regions (e.g. catchment basins). These regions can be then merged from previously identified markers belonging to the pores, the solid or the pore/solid mixture. The result of this segmentation is illustrated on Fig. 6. This segmentation clearly reveals the preferential orientation of pores with size ranging from 1 nm to 100 nm and from 1 to 800 nm (data not shown) related to the compaction axis, parallel and perpendicular, respectively. For this image, which is representative of an intermediate magnification, the segmentation gives 20% of pores, 41.7% of solid and 38.3% of pore/solid mixture. Taking into account these proportions and assuming a specific porosity of 100% for pores, 0% for solid and 50% for the pore/solid mixture (which could correspond to an average pore/solid mixture), a total porosity of 39% is obtained; this is in a good agreement with the expected bulk porosity of the compacted IDP. This argument tends to validate our segmentation procedure, allowing the detection of pores at a nanometer local scale.

### 3.2.3. 3D quantitative spatial distribution of the porosity

Using image stacks obtained either in SE or EsB mode with FIB-nT we visualize the pore space (pure black to low grayscale) from the surrounding and brightest clay matrix. Comparing the two types of imaging mode was illustrated in Fig. 7. Recent studies

[15,16] related to the microstructure of clay materials, based on image analysis, were proposed by mainly considering SE images to threshold the pore network. This choice was supported by a better contrast between pores and surrounding materials and a better signal to noise ratio than with the BSE images. On the other hand, using an energy selective BSE detector (EsB) improves the signal to noise ratio of the images, the contrast and the lateral/in depth resolution to a greater extent. Note that stripe artefacts are negligible with EsB in comparison to SE as the emission volume of quasi-elastic BSE is drastically reduced, to be small enough to limit the impact of topography. In order to demonstrate the use of the EsB-based BSE images rather than the SE images, a classically used thresholding method based on the Otsu approach [53] was applied on both type of images (Fig. 7). The accuracy of the pore recognition was verified by superimposing the outline of the pores (in red, Fig. 7) onto the images. It is obvious that more pores have been detected with the EsB-based approach. The SE images only detected the largest and isolated pores having a high grayscale contrast with the background. However, though EsB images improve the detection of pores, the smallest ones cannot be segmented by using such simple automatic routines. In this work, an image analysis procedure based on a method proposed in Ref. [54] on tomographic images was developed to extract the smallest pores having size close to the voxel size (5 nm). These pores are composed of pixels having an intermediate grayscale between pure black (void) and a

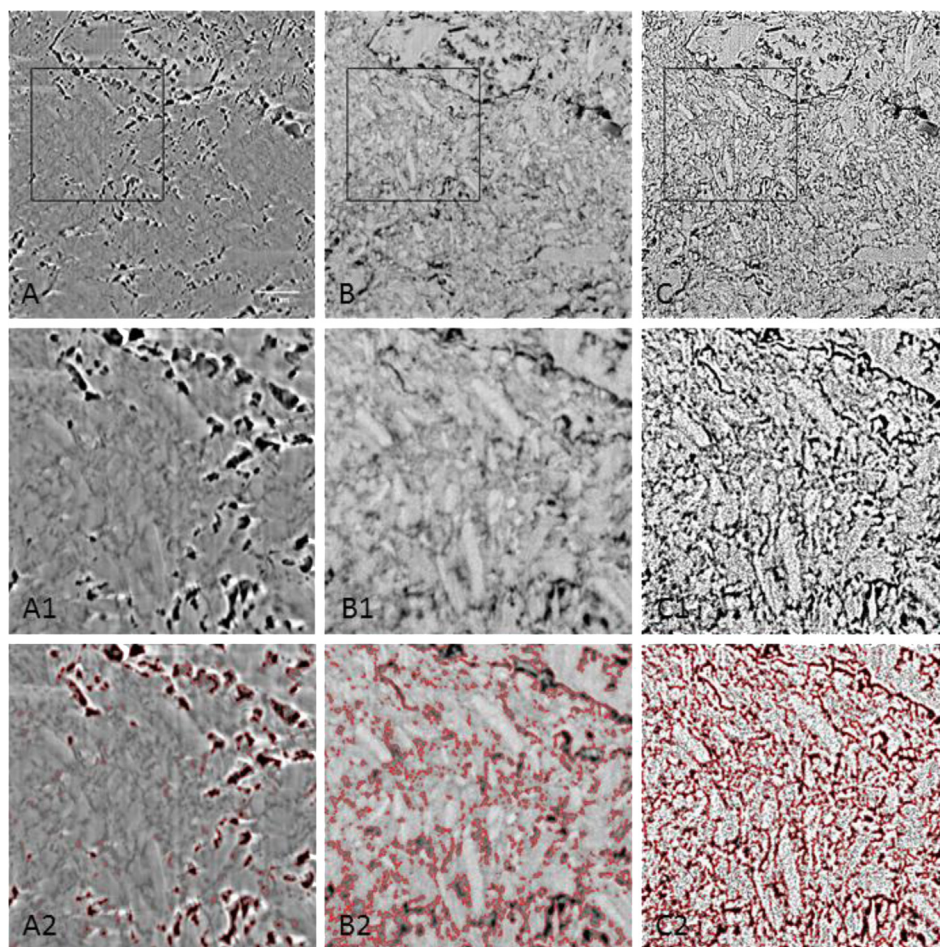


**Fig. 7.** SEM images of the compacted IDP with the same x,y coordinates. A and B images are SE and EsB images thresholded by the Otsu method. C images represent the method proposed in this work to improve the segmentation of the smallest pores. The red outlines represent the borders of the pores recognized according the type of images (SE or EsB) and thresholding. The final result of the method proposed in this work is C2. (For interpretation of the references to color in this figure legend, the reader is referred to the web version of this article.)

background gray value as the emission volume of EsB electrons (lower than 5 nm based on Monte Carlo simulations) corresponds to a mixture of pores filled with resin and the neighboring illite crystals. To separate these pores from the surrounding clay matrix, the maximum gradient magnitude, which is equivalent to the point of inflection of the smooth intensity profile across the interface (due to the insufficient resolution), was enhanced by optimizing the edge of transition between pores and clay grains. The sharp transition of the grayscale profile across the solid/pore interface is restored from the actual smooth profile by using a local weighted filter. This sharpening filter does not transform the edge position of the object but improves sharpness by increasing the acutance [54], although resolution remains the same (Fig. 7). Pores were then segmented using a watershed algorithm [55]. The watershed separations (markers belonging to the pores and solid) were selected by identifying the slope change of the gray level histogram on its first derivative [18,19] (data not shown). This segmentation procedure was successfully applied to the EsB image stack (Fig. 7). Fig. 8 displays a 3D visualization of the volume obtained from EsB FIB-nt (A). The pore space segmented using our image analysis procedure was superimposed to the EsB volume (in yellow, B) and illustrated alone on Fig. 8C. Secondly, Otsu thresholding (blue pores) was applied on the same EsB volume to illustrate the difference in mesopore network segmented according to the two methods (Fig. 8D). A region of interest (ROI) was also selected to demonstrate this difference (Figs. 8D and 9A and B). Otsu thresholding only depicts the largest and isolated pores (blue) while our proposed method is able in addition to detect a larger number of smaller pores. Fig. 9 focalizes on a ROI with just a few large pores to illustrate the importance in detecting smaller pores. The additional smallest pores in yellow (Fig. 9C) correspond to throats in between

the largest blue mesopores (Fig. 9D). Their detection substantially changes the connectivity and geometry of the mesopore network recognized.

From the pore network extracted using this image analysis procedure, a porosity of 28% was determined on a FOV of  $5 \times 5 \times 1 \mu\text{m}$ , which is representative when considering the RVE estimated from TEM images. This corresponds to 70% of the total bulk porosity of the sample, as illustrated by the maximum value of the cumulative PSD after normalization to the total bulk porosity (Fig. 10). In comparison, the pore network obtained using the Otsu thresholding applied on the same volume represents only 30% of the total porosity (Fig. 10). But the main difference between these methods is the connectivity of the pore network. With the classic Otsu method, only isolated pores are segmented with a positive Euler characteristic ( $\chi = 4242$ ), as was already mentioned in previous studies [15], while when detecting the connected pores by using a geodesic dilation from the external border of the image, the mesopore network recognized by the method proposed in this work is connected at 90% with a highly negative Euler characteristic ( $\chi = -53,071$ ).

#### 3.2.4. Pore size distribution

A large number of methods exist for determining PSD from cross-sectional 2D images. In this study, the classical intercept length (L) distribution method (or chord-length distribution) [56–59] was used to assess PSD on 2D thresholded TEM images. The intercepts are defined by the intersection of lines with the pore-solid interface. Here thresholded pore/solid mixtures have been merged with solids as the pixels detected as mixtures through the thickness TEM lamellae do not permit a robust estimation of pore size. Both clay particle orientation and pore size distributions

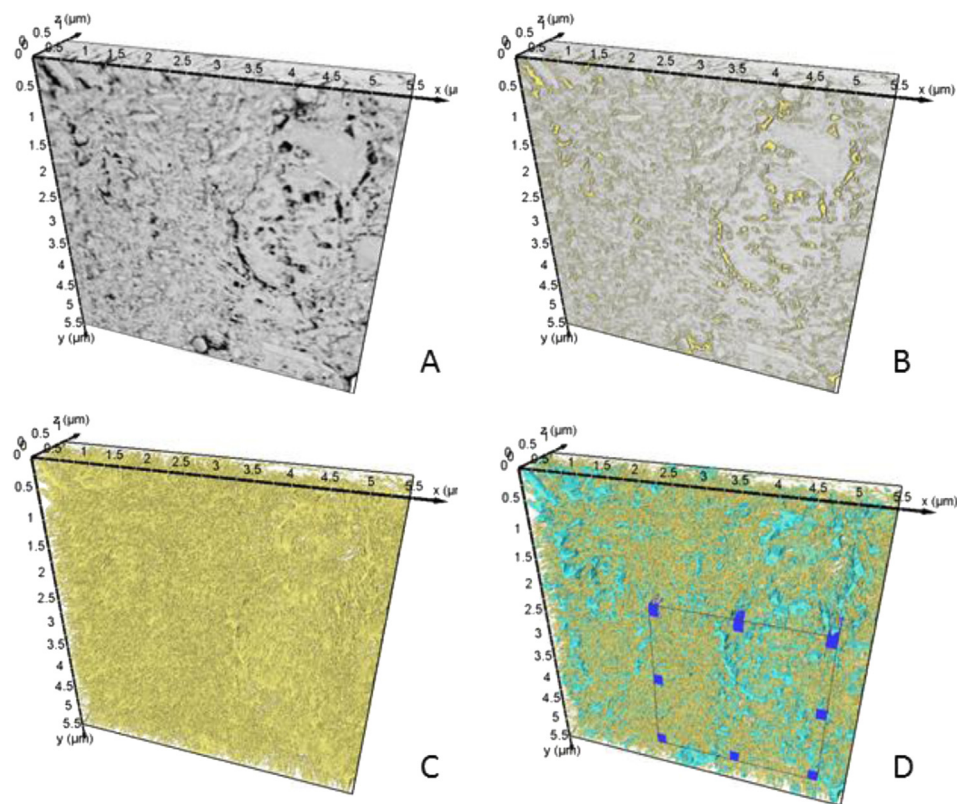


**Fig. 8.** 3D visualization of the BSE FIB-nt stack images (A). (B) Segmentation of the porosity (yellow). (C) Pore volume segmented from the method developed in this work. (D) Superimposition of the porosity segmented with Otsu thresholding (blue). (D) A region of interest (ROI) is placed on the volume to illustrate the difference between the two approaches in Fig. 9. (For interpretation of the references to color in this figure legend, the reader is referred to the web version of this article.)

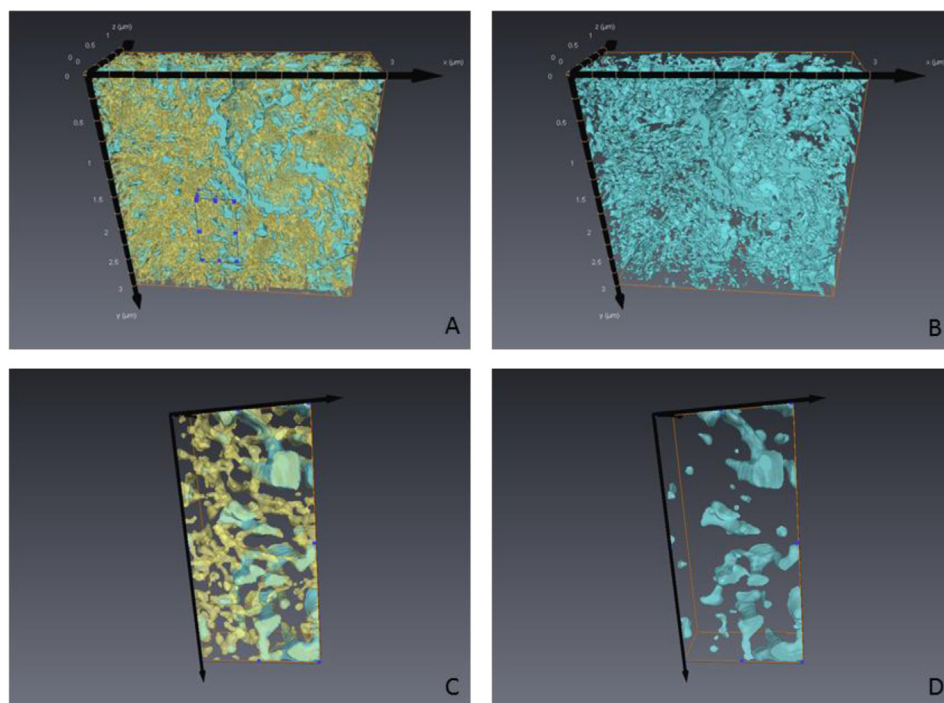


**Fig. 9.** Region of interest (ROI) illustrating the pores segmented from Otsu thresholding (B, light blue) and the method developed in this work (A, yellow). The ROI superimposed in (A) illustrates that the yellow pores mainly represent the throats (C and D). (For interpretation of the references to color in this figure legend, the reader is referred to the web version of this article.)

are known as transverse isotropic with clay particles mainly oriented perpendicular to the compaction axis and pores elongated in the same plane [60]. The smallest aperture of the pores is thus probed in a direction parallel to the compaction axis. The intercept length distribution was calculated along the Y-axis of the image almost parallel to the compaction axis in order to analyze the thinnest section of the mesopores. The intercept length ( $L$ ) distribution was then converted into a volume ( $V$ ) weighted PSD using the relationship given by Krohn (1988). Beyond the fact that this method is relatively basic, the implementation of a more complex method was not considered as 2D TEM projections are biased by

mixture effects along the electron beam axis. PSD based on intercept length distributions are given in Fig. 10.

PSD were also determined from the 3D spatial distribution of pores extracted from the EsB FIB-nt stack and the previously described segmentation procedure. Contrary to the discrete PSD calculated from the 2D TEM images with mixture pixels, a more robust continuous 3D PSD can be calculated from the 3D FIB-nt pore network [61] avoiding thus a 2D slice by slice integration. PSD were retrieved by determining the aperture diameter map [62], where the local aperture diameter is defined in any voxel. PSD were determined on both pore networks segmented by the classic Otsu method and the method proposed in this work. Such a local aperture corresponds to the maximal ball diameter centered on each voxel distant from the neighboring pore walls that is also involved when creating a curved interface between liquid  $N_2$  or Hg and air in slit- or tube-shaped pores. Therefore, when deriving from the Laplace's law, Kelvin and Washburn equations in order to calculate PSD from  $N_2$  adsorption or MIP data, we expect similar results. For both methods, PSD are similar down to a diameter of 30 nm; below that they diverge. The PSD deduced from the Otsu thresholding exhibits asymptotic behavior corresponding to a diameter limit of 30 nm where pores cannot be fully identified. On the other hand, PSD deduced from the method presented in this work is continuous until the resolution limits (i.e. 5 nm). The PSD obtained from FIB-nt images, TEM images and those acquired using bulk measurement ( $N_2$  adsorption and MIP interpreted by the XDQ program) are also the same range of pore size, even if some differences are still remaining, highlighting the overall reliability of the proposed methodology (Fig. 10). The main difference is due to limitations in the pore diameters that can be detected. Pore diameters below the voxel size (<5 nm) could not be segmented whereas mesopores down to 2 nm are accounted for in the BJH/ $N_2$  approach.

Based on the method proposed in this work, the PSD displays a continuous distribution between the largest and the smallest pore

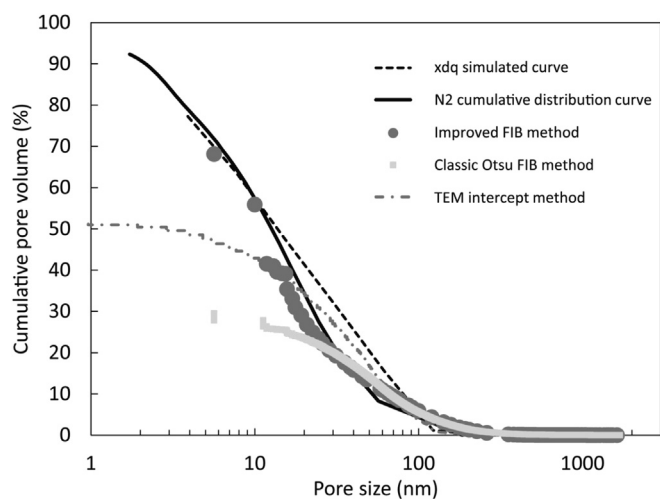


**Fig. 10.** Pore size distribution (PSD) of the compacted IDP calculated with the different methods (bulk and imaging). The PSD calculated from the 3D FIB-nt volume is given according the two methods discussed (this work and Otsu thresholding).

ranging from 5 to ~100 nm in which ~90% of the segmented pore network is connected. Such continuous PSD reflects the wedge-shaped morphology of mesopores. Still the unprobed mesopores in the 2–5 nm range probably fully connect the mesopores together. The main difference with a classic Otsu thresholding described in many recent studies [15,16], that only gives access to a small part of the mesopores (30%), is that detecting the mesopores down to 5 nm drastically impacts the geometry of the network and its connectivity through throat detection. This is in good agreement with the PSD obtained upon Hg intrusion, which provides an estimation of throat apertures that are mainly below 10 nm. High resolution 2D TEM images do not show the smallest pores as the projection through the TEM lamellae also limits the resolution.

### 3.2.5. 3D geometrical characterization

In addition to the classical pore volume and PSD determination, 3D geometrical characterizations of FIB-nt 3D pore networks were performed to better evaluate the anisotropy of the compacted illite material. The calculations were done on a specific ROI (Fig. 11) cropped from pore networks segmented by (1) the Otsu thresholding and (2) the method proposed in this work. The public-domain software iMorph (<http://imorph.fr/>) was used to perform a set of 3D morphometric and orientation analyzes. Firstly, a 3D visualization of the individual components constituting the pore network (one color represents one connected pore volume) confirms that the pore volume extracted using the segmentation method proposed in this work constitutes a continuum network, where 90% of the pore volume is connected, by contrast with the one extracted by the Otsu thresholding, which is made by several isolated pores (only 50% of the pore volume is connected).

The overall anisotropy of the pore space segmented by the proposed approach was evaluated using the mean intercept length (MIL) method [63]. The general principle of intercept lengths has been previously described in §3. The MIL calculated for the three

**Table 1**

Macroscopic and morphologic description of the segmented-pore network of compacted IDP.

Pore volume	The present work
Porosity (–)	0.28
Specific surface ( $\text{m}^2/\text{m}^3$ )	$3.5 \cdot 10^7$
Cells mean aperture diameter	78
Throat mean aperture diameter	9
Half axis length of the equivalent ellipsoid (nm)	
a	14
b	5
c	35
Mean Interception length (nm)	
X	6.1
Y	5.3
Z	6.9

main directions X, Y, Z is given in Table 1. The mean lengths toward the Z and X direction, which correspond to the axis in a plane perpendicular to the compaction direction, are higher than for the compaction axis (Y direction).

After separating each pore from its neighbor by detecting the throat, particle shape analysis was applied to each point of the connected pore space (Fig. 11c) by calculating the local inertia matrix for a voxel cloud centered on a point, from which three orthogonal vectors defining an ellipsoid (a, b, c) are calculated [64]. The local shape centered on a point was obtained by a front propagating technique which can lead to geodesic distance computation. The means of principal vectors calculated from each pore are longer in the X and Z directions than in the Y direction (Table 1). The 3D visualization of the local shape index of the pores (Fig. 11c) with the a/b elongation ratio [64] indicates also that the pore volume is mainly composed of pores with flattened shapes (i.e. wedge shaped) and throats in between. The mean aperture diameter of throats and pores (i.e. cells) is given in Table 1.

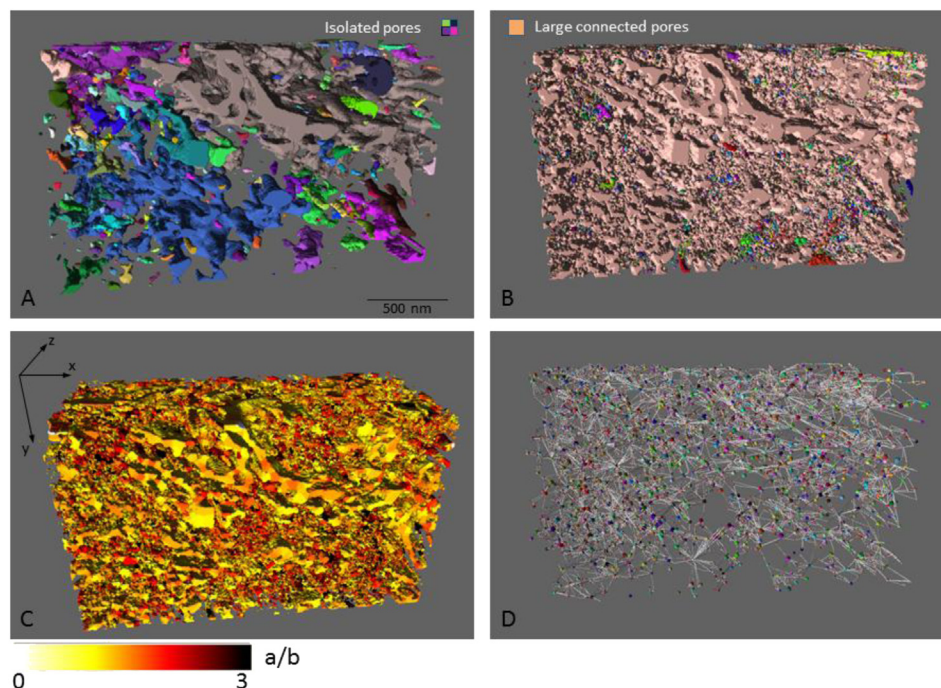


**Fig. 11.** 3D visualization of a ROI of  $400 \times 240 \times 180$  voxels. (A) individual pore components segmented from Otsu thresholding. Each color represents a pore not connected to the others. (B) Pore components segmented from this work. (C) Local shape classification from the computed half-axis length. The color palette indicates the a/b values. (D) Skeleton representation of the pore space. (For interpretation of the references to color in this figure legend, the reader is referred to the web version of this article.)

Finally, the tortuosity of the pore volume was calculated based on the pore network skeleton. Distance Ordered Homotopic Thinning combined with a fast marching method [65] were used to obtain the 3D skeleton and thus the graph of the pore structure (Fig. 11d). Tortuosity values are also deduced from geodesics calculations [66]. The results show that tortuosity depends on direction, where in the X, Z direction tortuosity is close to 1 while in the Y direction (parallel to the axis of compaction) the tortuosity is at 1.2, which is in good agreement with the three-dimensional model proposed by Matyka and Koza [67], according to the considered porosity. These results confirm that the pore volume organization is slightly anisotropic with a preferential orientation of the flat clay particles perpendicular to the axis of compaction.

#### 4. Discussion

The PSD and geometrical features of the pore network constitute key parameters governing the migration of fluid and solvate chemical elements through the clay formations. Though the solute transport is well characterized at the macroscopic scale thanks to diffusion experiments [6–9], modeling approaches at the pore and pore network scales based on actual geometry are scarce for clay-rocks. These are still required to build up a robust bottom-up strategy supporting the understanding of the diffusion-driven processes in clay-rocks at the scale of a radioactive waste repository. From actual pore spaces provided by imaging techniques (FIB-nt) [10,13–16] we can image the nanometric scale organization of clay materials but without detecting the smaller throats connecting the network. These data are currently suitable for modeling gas transfer since that is mainly related to the largest pore distribution, but do not allow modeling of solute or water diffusion processes requiring the complete spatial distribution of pores including the smallest as the throats.

In this work, we demonstrate that reliable recognition of the pore network including throat detection of clay materials based on FIB-nt and TEM techniques is feasible only by improving data acquisition and segmentation. Such optimization deeply affects the geometric and morphological parameters extracted (e.g. tortuosity, connectivity, PSD) and is needed to address robust modeling tasks in the future.

The studied material was a compacted clay material ( $\rho_d = 1.7$ ) mainly composed of illite (>90%). With this compacted clay plug we were able to work on a homogeneous system with controlled porosity with a negligible clay interlayer contribution. This facilitated the comparison between bulk and imaging techniques. Illite was also chosen to represent an analog system mimicking clay-rocks. All the techniques used in this work, whether bulk or microscopic, show that results converge to a similar and full PSD. The main improvement of this work was to demonstrate how the resolution limitations of FIB-nt techniques could be by-passed. By this improvement, we were able to detect more than 70% of the porosity, by contrast with recent works [15,16] demonstrating that only less than 20% could be detected. To detect more than 20% of the pore volume, an image analysis procedure was proposed. This procedure was mainly based on a sharpening effect that was applied to segment pores having different sizes, even those close to the voxel size. This upstream work has improved the detection of pores and allowed the segmentation of an interconnected pore network. In addition to FIB-nt imaging, 2D TEM analysis gives complementary data allowing the reliability of the results provided by FIB-nt to be cross-checked and to go further in the characterization of the nanoscale by imaging the clay particle morphology and structure. This study also pinpoints the limitations of 2D TEM imaging for representing the spatial distribution of pores at nanoscales in comparison to FIB-nt, which constitutes a key technique

for addressing these topics. Direct analysis of the grayscale TEM images can nevertheless give quantitative information about geometrical features of the organization (anisotropy, RVE, etc.).

Applying geometrical characterizations of the pore spatial distributions extracted from FIB-nt and TEM imaging has demonstrated the preferential orientation of pores perpendicular to the compaction for the compacted illite material. The effect of the preferred pore orientation was also quantified towards the tortuosity of the pore pathways and leads to an anisotropy feature. This anisotropy of the pore network is expected to induce anisotropic transfer behavior in the clay matrix of clay-rock even if a part of the anisotropy is due to the preferential orientation of non-clay grains [20].

A comparison between the PSD extracted from FIB data and those determined from bulk measurements, mainly  $N_2$  adsorption and MIP, reveals that they are in the same range in terms of pore size even if some differences exist in particular with the MIP PSD. Such discrepancies between the PSD determined based on from  $N_2$  adsorption and MIP have already been discussed for mesoporous silica, revealing that the PSD calculated from gas condensation techniques either mercury intrusion are similar and valid only for a given geometry of the pores [68]. The overall overestimation or underestimation of the pore size using MIP can be attributed to the effect of surface roughness or defects [69] on the mercury contact angle, which is larger for a rough surface than for a plane surface while the surface defect does not affect the mesopore size by nitrogen adsorption. The pore size and shape are assuredly important in the determination of the pore size distribution and the good agreement between the different technics.

#### 5. Conclusion

The originality of this work lies in combining several imaging techniques (FIB-nt and TEM), image analysis methods, and bulk measurements to quantify the pore space geometry of a compacted illite clay material. The consistency of the data provided for each approach was analyzed based on specific work dedicated to the characterization of pore size distribution (PSD). The main result of this work is a 3D pore distribution extracted from FIB-nt data and a dedicated image analysis procedure encompassing the full PSD of a compacted illite material. The morphological and geometrical analysis calculated from TEM and FIB-nt images also shows the anisotropy structure of the compacted IDP sample.

Our other main achievement was that we tackled the limitations in FIB-nt resolution described by many authors using an optimized procedure combining image acquisition and image segmentation methods based on morphological techniques. From the proposed approach we identified more than 70% of the total porosity of the sample. Moreover, beyond this, we saw that most of the pores are connected in 3D. The purified and homogeneous illite sample used is fully adapted for cross-comparison of the different PSD provided by different techniques. The good agreement between all the PSD demonstrates the robust image acquisition and treatments used in this work. As a result, exactly the same image acquisition and analysis approach by FIB-nt could be now applied with confidence to any other more complex heterogeneous clay materials to obtain relevant pore network characterization for the probed volume.

The next step is to perform direct numerical simulation in the actual 3D pore network extracted as part of this study to identify several transfer properties (diffusion coefficients, diffusion anisotropy, and diffusion tortuosity). The goal will be to understand the impact of the spatial distribution of the pores and microstructure on the diffusion parameter to better understand how a solute migrates through a clay-rich formation and to propose realistic transfer modeling from the pore network to the pore scale.

## Acknowledgments

This research received funding from the European Atomic Energy Community Seventh Framework Programme [FP7 – Fission – 2009] under grant agreement no. 249624, Collaborative Project Catclay and from the French ANR SIMISOL (ANR-009-SYSC-012). We thank Frédéric Charlot and Fabienne Warmont for the acquisition of FIB-nt data and TEM images, respectively.

## References

- [1] S. Altmann, C. Tournassat, F. Goutelard, J.C. Parneix, T. Gimmi, N. Maes, *Appl. Geochem.* 27 (2012) 463–478.
- [2] M.H. Bradbury, B. Baeyens, *Appl. Clay Sci.* 52 (2011) 27–33.
- [3] S. Sammartino, M. Siitari-Kauppi, A. Meunier, P. Sardini, A. Bouchet, E. Tevissen, *J. Sediment. Res.* 72 (2002) 937–943.
- [4] B. Yven, S. Sammartino, Y. Gérard, F. Homand, F. Villieras, *Mémoires la Société Géologique Fr.* 178 (2007) 73–90.
- [5] S. Sammartino, A. Bouchet, D. Pret, J.C. Parneix, E. Tevissen, *Appl. Clay Sci.* 23 (2003) 157–166.
- [6] T. Melkior, S. Yahiaoui, D. Thoby, S. Motellier, V. Barthes, *Phys. Chem. Earth* 32 (2007) 453–462.
- [7] M.A. Glaus, S. Frick, R. Rosse, L.R. Van Loon, *Geochimica Cosmochimica Acta* 74 (2010) 1999–2010.
- [8] T. Gimmi, G. Kosakowski, *Environ. Sci. Technol.* 45 (2011) 1443–1449.
- [9] P. Jacquier, D. Hainos, J.C. Robinet, M. Herbet, B. Grenut, A. Bouchet, C. Ferry, *Appl. Clay Sci.* 83 (2013) 129–136.
- [10] G. Desbois, J.L. Urai, P.A. Kukla, *eEarth* 4 (2009) 15–22.
- [11] S. Gaboreau, C. Lerouge, S. Dewonck, Y. Linard, X. Bourbon, C.I. Fialips, A. Mazurier, D. Pret, D. Borschneck, V. Montouillout, E.C. Gaucher, F. Claret, *Am. J. Sci.* 312 (2012) 314–356.
- [12] S. Gaboreau, D. Pret, E. Tinseau, F. Claret, D. Pellegrini, D. Stammose, *Appl. Geochem.* 26 (2011) 2159–2171.
- [13] L. Holzer, B. Munch, M. Rizzi, R. Wepf, P. Marschall, T. Graule, *Appl. Clay Sci.* 47 (2010) 330–342.
- [14] M.E. Houben, G. Desbois, J.L. Urai, *Mar. Pet. Geol.* 49 (2014) 143–161.
- [15] L.M. Keller, L. Holzer, R. Wepf, P. Gasser, B. Munch, P. Marschall, *Phys. Chem. Earth* 36 (2011) 1539–1544.
- [16] L.M. Keller, P. Schuetz, R. Erni, M.D. Rossell, F. Lucas, P. Gasser, L. Holzer, *Microporous Mesoporous Mater.* 170 (2013) 83–94.
- [17] D. Pret, *Nouvelles méthodes quantitatives de cartographie de la minéralogie et de la porosité dans les matériaux argileux: application aux bentonites compactées des barrières ouvragées* [PhD thesis], Université de Poitiers, France, Poitiers, 2003, p. 257.
- [18] D. Pret, S. Sammartino, D. Beaufort, M. Fialin, P. Sardini, P. Cosenza, A. Meunier, *Am. Mineral.* 95 (2010) 1389–1398.
- [19] D. Pret, S. Sammartino, D. Beaufort, A. Meunier, M. Fialin, L.J. Michot, *Am. Mineral.* 95 (2010) 1379–1388.
- [20] J.C. Robinet, P. Sardini, D. Coelho, J.C. Parneix, D. Pret, S. Sammartino, E. Boller, S. Altmann, *Water Resour. Res.* 48 (2012).
- [21] P. Sardini, A. El Albani, D. Pret, S. Gaboreau, M. Siitari-Kauppi, D. Beaufort, *J. Sediment. Res.* 79 (2009) 584–592.
- [22] G.R. Chalmers, R.M. Bustin, I.M. Power, *AAPG Bull.* 96 (2012) 1099–1119.
- [23] N.K. Tovey, M.W. Hounslow, *J. Geol. Soc.* 152 (1995) 119–129.
- [24] P.C. Baveye, M. Laba, W. Otten, L. Bouckaert, P. Dello Sterpaio, R.R. Goswami, D. Grinev, A. Houston, Y. Hu, J. Liu, S. Mooney, R. Pajor, S. Sleutel, A. Tarquis, W. Wang, Q. Wei, M. Sezgin, *Geoderma* 157 (2010) 51–63.
- [25] F. Claret, B.A. Sakharov, V.A. Drits, B. Velde, A. Meunier, L. Griffault, B. Lanson, *Clays Clay Miner.* 52 (2004) 515–532.
- [26] I. Djeran-Maigre, D. Tessier, D. Grunberger, B. Velde, G. Vasseur, *Mar. Pet. Geol.* 15 (1998) 109–128.
- [27] M.H. Bradbury, B. Baeyens, *Geochimica Cosmochimica Acta* 73 (2009) 990–1003.
- [28] A. Meunier, B. Velde, *Illite: Origins, Evolution and Metamorphism*, Springer, 2004.
- [29] V. Gabis, *Bull. de la Société Française de Minéralogie Cristallogr.* 86 (1963) 315–354.
- [30] B. Baeyens, M.H. Bradbury, *J. Contam. Hydrol.* 27 (1997) 199–222.
- [31] E. Gaucher, C. Robelin, J.M. Matray, G. Negral, Y. Gros, J.F. Heitz, A. Vinsot, H. Rebours, A. Cassagnabere, A. Bouchet, *Phys. Chem. Earth* 29 (2004) 55–77.
- [32] D. Pret, P. Sardini, D. Beaufort, R. Zellagui, S. Sammartino, *Appl. Clay Sci.* 27 (2004) 107–118.
- [33] K.S.W. Sing, *Colloid Surf. A* 241 (2004) 3–7.
- [34] G. Gallé, *Cem. Concr. Res.* 31 (2001) 1467–1477.
- [35] E.P. Barrett, L.G. Joyner, P.P. Hallenda, *J. Am. Chem. Soc.* 73 (1951) 373–380.
- [36] S.J. Gregg, K.S.W. Sing, *Adsorption, Surface Area and Porosity*, second ed., Academic Press London, 1982, p. 303.
- [37] E.W. Washburn, *Phys. Rev.* 17 (1921) 273–283.
- [38] R.G. Jenkins, M.B. Rao, *Powder Technol.* 38 (1984) 177–180.
- [39] R.A. Cook, K.C. Hover, *Cem. Concr. Res.* 29 (1999) 933–943.
- [40] K. Xu, J.F. Daian, D. Quenard, *Transp. Porous Med.* 26 (1997) 319–338.
- [41] K. Xu, J.F. Daian, D. Quenard, *Transp. Porous Med.* 26 (1997) 51–73.
- [42] L. Holzer, F. Indutnyi, P.H. Gasser, B. Munch, M. Wegmann, *J. Microscopy Oxford* 216 (2004) 84–95.
- [43] P. Maillard, *Photogramm. Eng. Remote Sens.* 69 (2003) 357–367.
- [44] S.R. Sternberg, *Biomed. Image Process. Comput.* 16 (1983) 22–34.
- [45] T. Prill, K. Schladitz, D. Jeulin, M. Faessel, C. Wieser, *J. Microsc.* 250 (2013) 77–87.
- [46] P. Thevenaz, U.E. Ruttimann, M. Unser, *IEEE T Image Process* 7 (1998) 27–41.
- [47] G. Carpentier, *FFTRemoveStreaks macro for removing interference streaks from confocal images*, ImageJ News (4 November 2004) v1.330.
- [48] C.E. Woodcock, A.H. Strahler, D.L.B. Jupp, *Remote Sens. Environ.* 25 (1988) 349–379.
- [49] F. Bron, F. Jeulin, *Image Anal. stereol.* 23 (2004) 33–44.
- [50] W.J. Druggan, J.R. Willis, *J. Mech. Phys. Solids* 44 (1996) 497–524.
- [51] M. Galli, J. Cugnoni, J. Botsis, *Eur. J. Mech. A Solids* 33 (2012) 31–38.
- [52] S. Beucher, C. Lantuejoul, *Use of Watersheds in Contour Detection*, International Workshop on Image Processing, Real Time Edge and Motion Detection/estimation, Rennes, 1979.
- [53] N. Otsu, *IEEE T Syst. Man. Cyber* 9 (1979) 62–66.
- [54] A.P. Sheppard, R.M. Sok, H. Averdunk, *Phys. A Stat. Mech. Appl.* 339 (2004) 145–151.
- [55] L. Vincent, P. Soille, *Pattern Analysis Mach. Intell.* 13 (1991) 583–598.
- [56] C.E. Krohn, *J. Geophys. Res. Solid Earth Planets* 93 (1988) 3286–3296.
- [57] S. Torquato, B. Lu, *Phys. Rev. E* 47 (1993) 2950–2953.
- [58] O. Rozenbaum, S.R. du Roscoat, *Phys. Rev. E* 89 (2014) 11.
- [59] P. Levitz, D. Tchoubar, *J. Phys. I Fr.* 2 (1992) 771–790.
- [60] F. Hubert, I. Bihannic, D. Pret, E. Tertre, B. Nauleau, M. Pelletier, B. Deme, E. Ferrage, *Clays Clay Miner.* 61 (2013) 397–415.
- [61] B. Munch, L. Holzer, *J. Am. Ceram. Soc.* 91 (2008) 4059–4067.
- [62] J.F. Delerue, E. Perrier, Z.Y. Yu, B. Velde, *Phys. Chem. Earth* 24 (1999) 639–644.
- [63] J. Vicente, J.V. Daurelle, G. Brossard, A. Blom, A. Douteur, Y. Delmotte, E. Brun, *Chem. Eng. Sci.* 72 (2012) 172–178.
- [64] E. Brun, J. Vicente, in: B.M. Dawant, D.R. Haynor (Eds.), *Medical Imaging 2010: Image Processing*, Spie-Int Soc Optical Engineering, Bellingham, 2010.
- [65] J.A. Sethian, *Level Set Methods and Fast Marching Methods*, Cambridge, 1999.
- [66] E. Brun, J. Vicente, F. Topin, R. Occelli, *Geometrical Measurement of Real Foams from 3D Images*, Destech Publications, Inc, Lancaster, 2008.
- [67] M. Matyka, Z. Koza, *AIP Conf. Proc.* 1453 (2012) 17–22.
- [68] A. Galarneau, B. Lefevre, H. Cambon, B. Coasne, S. Valange, Z. Gabelica, J.-P. Bellat, F. Di Renzo, *J. Phys. Chem. C* 112 (2008) 12921–12927.
- [69] J. Iapichella, J.-M. Meneses, I. Beurroies, R. Denoyel, Z. Bayram-Hahn, K. Unger, A. Galarneau, *Microporous Mesoporous Mater.* 102 (2007) 111–121.